RSC Advances

PAPER

View Article Online
View Journal | View Issue

Cite this: *RSC Adv.*, 2019, **9**, 7181

Influence of morphology of monolithic sulfur–poly(acrylonitrile) composites used as cathode materials in lithium–sulfur batteries on electrochemical performance†

Tim Lebherz,[ab] Martin Frey,[c] Andreas Hintennach[b] and Michael R. Buchmeiser *[ad]

Received 4th December 2018
Accepted 25th February 2019

DOI: 10.1039/c8ra09976f

rsc.li/rsc-advances

Solvent-induced phase separation (SIPS) and thermally-induced phase separation (TIPS) derived poly(acrylonitrile) (PAN) based monoliths with different morphology and specific surface area were prepared and thermally converted into monolithic sulfur–poly(acrylonitrile) (SPAN) materials for use as active cathode materials in lithium–sulfur batteries. During thermal processing, the macroscopic monolithic structure fully prevailed while significant changes in porosity were observed. Both the monomer content in the precursor PAN-based monoliths and the tortuosity of the final monolithic SPAN materials correlate with the electrochemical performance of the SPAN-based cathodes. Overall, percolation issues predominate. In percolating SPAN-based cathode materials, the specific capacity of the SPAN-based cells increases with decreasing tortuosity. All monolithic SPAN materials provided highly reversible and cycle stable cathodes reaching reversible discharge capacities up to 1330 mA h g_{sulfur}^{-1} @ 0.25C, 900 mA h g_{sulfur}^{-1} @ 2C and 420 mA h g_{sulfur}^{-1} @ 8C.

Introduction

Lithium–sulfur batteries represent a promising post-Li-ion technology due to their high theoretical specific capacity of 1672 mA h g_{sulfur}^{-1} and high specific energy density of 2600 W h g^{-1}.[1,2] Sulfur itself is a non-toxic, readily available and cheap cathode material. The chemistry of a Li–S-cell is based on the reversible reaction of lithium with sulfur forming Li_2S according to $1/8S_8 + 2Li \rightarrow Li_2S$.[3]

However, there are still several issues that limit the practical use of lithium–sulfur batteries.[4] One is related to the mostly irreversible shuttling of polysulfides from the cathode to the anode. Thus, the reduction of elemental sulfur by elemental lithium occurs stepwise forming oligo-/polysulfides of the general formula Li_2S_x ($3 \leq x \leq 8$).[5] These intermediates are soluble in common ether-based electrolytes. As a result, the polysulfides are shuttling to the anode, where they are irreversibly reduced. In addition to the loss of active material, this results in a poor electrochemical efficiency of the cell and the formation of a passivating layer of Li_2S on the lithium anode. Another challenge is the insulating nature of elemental sulfur, which renders its usage without any modifications and/or conversion challenging. There exist numerous approaches to overcome this issue. These entail the impregnation of carbonaceous structures such as meso- and microporous carbon black,[6,7] carbon nanofibers[8] or multi-walled carbon nanotubes[9] with elemental sulfur. This method leads to active materials, which are resisive and render the sulfur electrochemically addressable. However, the sulfur is only physisorbed on the carbon materials, which becomes an issue in combination with electrolytes that are able to dissolve sulfur. Alternatively, a sulfur–poly(acrylonitrile) composite (SPAN), in which the sulfur is bound covalently to a condensed, polyaromatic backbone, has been developed.[10,11] Briefly, for SPAN synthesis, poly(acrylonitrile) (PAN) is reacted with elemental sulfur at elevated temperature, usually between 350 and 550 °C. The resulting composite contains up to 55 wt% of sulfur and possesses substantial electric conductivity.[10,12,13] We already presented a comprehensive structure of the composite that contains both thioamides and oligosulfide bridges (Fig. 1).[14–16]

Notably, the (vinylogous and phenylogous) thioamide groups within the structure are crucial since they function as anchoring groups for the formation of SPAN-S_x species ($2 \leq x \leq 8$) during reduction/oxidation, *i.e.* discharge/charge of the SPAN-matrix.[17] This reversible formation of polymer-bound oligomeric sulfur species is responsible for one of the major advantages of the SPAN-composites, which is the attenuation of the polysulfide

[a]*Institute of Polymer Chemistry, University of Stuttgart, 70569 Stuttgart, Germany. E-mail: michael.buchmeiser@ipoc.uni-stuttgart.de*
[b]*Daimler AG, RD/EBT, HPC G012-BB, 71034 Böblingen, Germany*
[c]*Daimler AG, RD/EBB, HPC X461, 71059 Sindelfingen, Germany*
[d]*German Institutes of Textile and Fiber Research (DITF) Denkendorf, 73770 Denkendorf, Germany*

† Electronic supplementary information (ESI) available: SEM images, sorption isotherms, pore size distributions, IR spectra and additional electrochemical results. See DOI: 10.1039/c8ra09976f

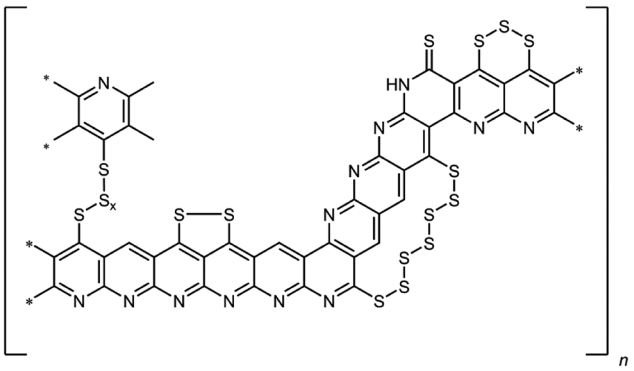

Fig. 1 Structural motifs in SPAN.

shuttle[18] due to the insolubility of SPAN and all intermediates.[17] Because of the absence of almost any soluble polysulfide intermediates the system also turned out to be compatible with $LiPF_6$/carbonate-based electrolytes,[19] which are commonly used for Li-ion batteries.

Finally, SPAN-based cathodes show substantially higher cycle stabilities and higher sulfur utilization (up to 90%)[20] than cathodes based on elemental sulfur.[1,17,21,22] One disadvantage of the SPAN-system, however, is related to its low sulfur loading of 40–55 wt% compared to cathodes based on elemental sulfur, which reach sulfur loadings up to 80 wt%.[1,12,17,21,23] Nonetheless, in combination with a dimethyl trisulfide (DMTS) based electrolyte, SPAN-based cathodes are still able to reach discharge capacities up to 4 mA h cm^{-2}.[24] Similar to the working mode of SPAN cathodes outlined above, the mechanism of such a Li/SPAN/DMTS hybrid cell involves a reversible interaction of the thioamides in the SPAN-structure with CH_3S_x-fragments of DMTS. The common method for the preparation of SPAN is the use of particulate PAN[10,14–16,25] but it is also possible to use PAN-based fibers, which offer the advantages of better processability, defined morphology and improved percolation, which in turn results in a better electrochemical performance compared to particulate SPAN.[26] In view of that, we considered monolithic SPAN a viable alternative material since it should be accessible with defined pore structure and offer sufficient percolation between the individual structure-forming microglobules. Generally, the synthesis of monolithic materials typically entails the copolymerization of a monomer and a crosslinker under solvent-induced phase separation (SIPS) conditions and results in the formation of a porous, three-dimensional polymeric network based on structure-forming microglobules in the micrometer range.[27–30] The specific surface areas and pore size distribution can be influenced by the synthetic parameters such as the amount and Hildebrand solubility parameters of the solvents, the temperature and the amount of initiator.[28] In addition to the synthesis *via* solvent-induced phase separation it is also possible to synthesize monoliths *via* thermally-induced phase separation (TIPS).[31,32] In contrast to a SIPS based approach, in TIPS there is no polymerization involved during monolith formation. The precursor itself is a polymer, which is dissolved in a solvent mixture at higher temperatures. TIPS occurs during the cooling of the solution, thereby delivering a non-crosslinked polymeric monolith. The structure of the resulting monolith can be influenced by the solvent system and the concentration of the dissolved polymer. Here, we present the first SPAN-based monoliths as active materials with defined morphology for use in lithium–sulfur batteries and present correlations between polymer content in the PAN monoliths, microglobule packing density, tortuosity as well as percolation and electrochemical performance.

Results and discussion

Synthesis and characterization of PAN-based monoliths

Four PAN-based monoliths (PAN-1 to PAN-4) were synthesized *via* SIPS applying reversible addition-fragmentation-chain transfer (RAFT) polymerization.[33] Acrylonitrile was used as monomer and ethyleneglycol dimethacrylate (EGDMA) as crosslinker. 2,2′-Azobis(2-methylpropionitrile) (AIBN) served as initiator, cyano-2-propyl dodecyl trithiocarbonate (CPDT) as RAFT-agent. Their concentration as well as the molar ratio of acrylonitrile : EGDMA (16 : 1) was kept constant. In order to achieve different porosities and morphologies, the amounts of the solvents used for the synthesis, *i.e.* ethanol (EtOH), and ethylene carbonate (EC) were varied (Table 1). Complementary, two PAN-based monoliths (PAN-5 and PAN-6) were synthesized *via* TIPS. Different amounts of PAN (M_n = 35 600 g mol^{-1}, PDI = 3.6, c(PAN) = 60 mg mL^{-1} and 120 mg mL^{-1}) were dissolved in DMSO : H_2O = 88 : 12 (vol/vol). After cooling of the solution, PAN-based monoliths were obtained. According to N_2-sorption measurements, all SIPS-derived PAN-monoliths possessed average pore diameters in the range of 30–50 nm and specific surface areas between 20 and 30 m^2 g^{-1} in case of the SIPS-based PAN-monoliths, whereas the TIPS-derived PAN-monoliths showed higher specific surface areas of 106 m^2 g^{-1} and 225 m^2 g^{-1} (Table S1, ESI†).

The difference in specific surface areas is attributed to the two different synthetic approaches to these two monolithic systems and to the different monomer content. Clearly, the freeze-drying process of the non-crosslinked TIPS-derived PAN-monoliths influences the resulting porosity of the monolith and generates a higher BET surface area. Scanning electron microscopy images of all monoliths showed a typical monolithic structure, consisting of agglomerated structure-forming microglobules (Fig. 2).

Synthesis and characterization of SPAN-monoliths

SPAN-monoliths were synthesized *via* reaction of S_8 with the polymeric monoliths PAN-1 to PAN-6 according to procedures

Table 1 Parameters for the synthesis of the four different PAN-monoliths

Monolith	m(monomers) : m(solvents)	Solvent system (EC/EtOH, wt%/wt%)
PAN-1	30 : 70	6 : 4
PAN-2	40 : 60	7 : 3
PAN-3	50 : 50	8 : 2
PAN-4	60 : 40	1 : 9

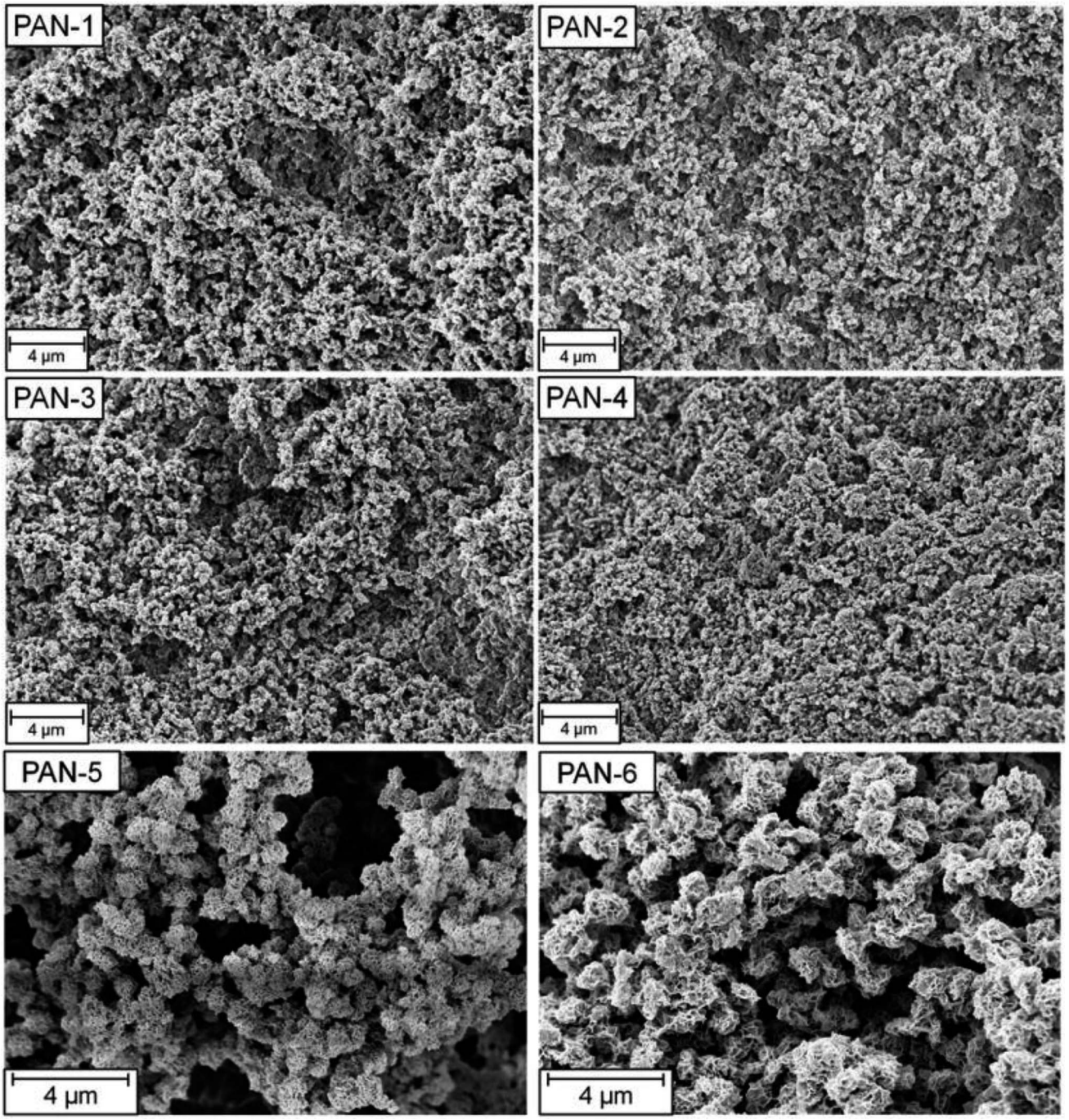

Fig. 2 SEM-pictures of the SIPS-derived PAN-monoliths PAN-1 to PAN-4 and the TIPS-derived PAN-monoliths PAN 5 and PAN 6.

described for pellicular SPAN.[26] The elemental composition of the materials was determined *via* elemental analysis and is summarized in Table 2.

All synthesized SPAN-monoliths showed an S-content around 40 wt%. The atomic C : H ratio was between 3.0 and 3.6 throughout. The high C : H ratio indicates substantial dehydrogenation during formation of the SPAN structure and, concomitant formation of the polyannelated, cyclic, nitrogen-containing backbone. Conversion of the PAN-based monolith into the SPAN-monolith was also monitored by IR-spectroscopy (Fig. S23 and S24, ESI†), which revealed the disappearance of the nitrile band and formation of the typical SPAN structure.[14–16] Thus, the spectra of the PAN-monoliths PAN-1 to PAN-6 showed one characteristic band, *i.e.* the nitrile stretching of the acrylonitrile at 2240 cm^{-1} and in case of the PAN-monoliths PAN-1 to PAN-4 in addition the ester band of the crosslinker at 1725 cm^{-1}. Both bands disappeared after reaction with elemental sulfur. The IR-spectrum of the SPAN-monolith showed only one strong broad band in the range of 1000–1600 cm^{-1}.

Table 2 Elemental composition, specific surface area, σ, average pore diameter, d_p, and pore volume, V_p, of monoliths SPAN-1 to SPAN-6

	SPAN-1	SPAN-2	SPAN-3	SPAN-4	SPAN-5	SPAN-6
C [%]	44.55	44.85	44.2	44.05	40.68	39.57
H [%]	1.09	1.24	1.18	1.11	1.02	0.91
N [%]	12.24	11.91	12.36	12.22	13.65	13.51
S [%]	38.8	38.9	39.4	40.6	38.4	40.8
O [%]	3.3	3.1	2.9	2.0	6.3	5.2
C : H (Atomic ratio)	3.40	3.01	3.12	3.31	3.34	3.61
C : N (Atomic ratio)	4.25	4.39	4.17	4.21	3.48	3.42
d_p [nm]	4.0	4.0	4.2	3.5	3.9	4.0
σ [$m^2\ g^{-1}$]	14	24	23	18	116	97
V_p [$cm^3\ g^{-1}$]	0.04	0.08	0.10	0.08	0.24	0.16

This band is characteristic for SPAN-materials and is caused by the vibrations of the condensed, aromatic, pyridine-like structure. The bands in the region of 600–900 cm^{-1} are most likely caused by the vibrations of the thioamide groups.[34] The absence of the adsorption bands of both the nitrile and the ester group indicates that both infiltration with liquid sulfur and thermally-induced conversion of PAN to SPAN was complete and the crosslinker was thermally eliminated. Clearly, both the elimination of the crosslinker and the dehydrogenation of the PAN during the conversion into SPAN generated small mesopores, which resulted into a decrease in the average pore diameter to approximately 4 nm (Fig. S7–S12, ESI†). Notably, despite the significant changes on the molecular level, conversion of PAN to SPAN occurred under retention of the macroscopic structure of the monolith, as shown in Fig. 3. SEM images of the SPAN-monoliths (Fig. S19–S21, ESI†) also confirmed the retention of the porous monolithic structure. Notably, this is one of the comparably rare examples for the conversion of a porous polymeric network into a carbonaceous one under full retention of both the microscopic and the macroscopic structure.[35,36]

Electrochemistry

Cyclic voltammetry (CV) was carried out in the range between 1 and 3 V. Fig. 4 shows the representative cyclic voltammogram of monolithic SPAN-4. The CVs of all active materials looked very similar. The first discharge cycle shows a broad signal with a maximum at 1.6 V and differs from all following cycles due to the irreversible reduction of the backbone of the SPAN-matrix.[17,37] This phenomenon is well known for SPAN-based cathode materials.[17,37] All following discharge cycles show the same curvature with a broad bimodal signal with maxima at

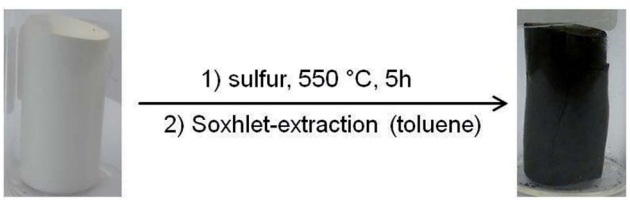

Fig. 3 Scheme of the conversion of a PAN- (left) into an SPAN-monolith (right).

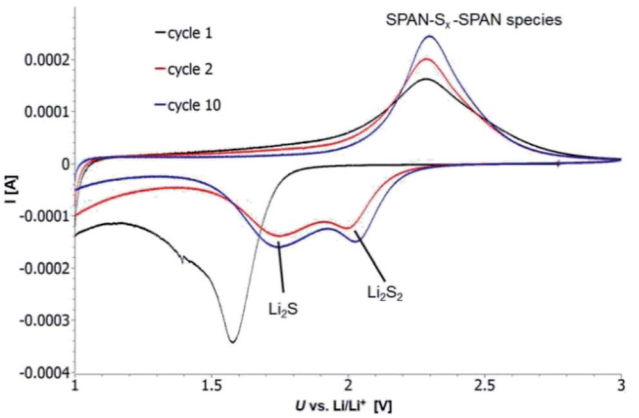

Fig. 4 Representative CV of a cell based on monolithic SPAN-4 as active material with 3 M LiTFSI in EC/DMC (1 : 1) as electrolyte *vs.* Li/Li^+. The cyclic voltammograms of the other active materials looked similar.

1.75 and 2.05 V, respectively.[38–40] These indicate the formation of Li_2S and Li_2S_2 according to SPAN-S_x + 2Li → Li_2S_y + SPAN-S_{x-y} with $2 \leq x \leq 7$ and $1 < y < 2$. All oxidation cycles in CV, including the first cycle, show a broad signal at 2.3 V which indicates the formation of SPAN-S_x-SPAN species according to SPAN-S_{x-1}-SPAN + Li_2S → SPAN-S_x-SPAN + 2 Li with $2 \leq x \leq 8$.[37,41] The performance of the Li/SPAN-system was tested in a symmetrical stress test. The Li–S-cells were charged and discharged at different C-rates, starting and ending with 0.25C and applying a maximum C-rate of 2C. The results of the symmetrical stress tests are shown in Fig. 5 and 6; the initial discharge capacities of the cells are summarized in Table 3. The best monolithic SPAN-material (SPAN-4) showed a high specific discharge capacity of 900 mA h g_{sulfur}^{-1} at 2C. In addition to these experiments we performed cycle tests with each active material with a charge/discharge rate of 1C (Fig. 7 and 8).

Even after 200 cycles, cells based on SPAN-2 to SPAN-4 showed only a minor loss in capacity (5%) and the coulombic efficiency of the cells was >99% throughout. This strongly suggests that in these cathode materials both the reduction and oxidation of the monolithic SPAN-matrices proceeds in a highly reversible manner, at least up to 200 cycles. By contrast, the TIPS-derived SPAN monoliths SPAN-5 and SPAN-6 showed high initial discharge capacities (Fig. 6, Table 3) but a more pronounced loss in discharge capacities within 200 cycles

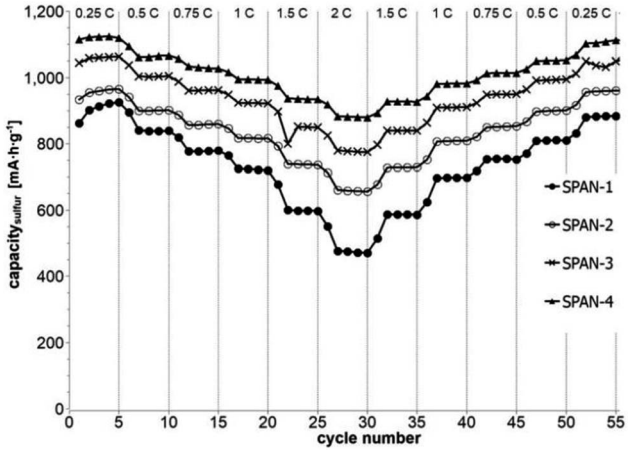

Fig. 5 Symmetrical stress test 0.25C–2C–0.25C of cells prepared from the SIPS-derived SPAN-based monoliths SPAN-1 to SPAN-4.

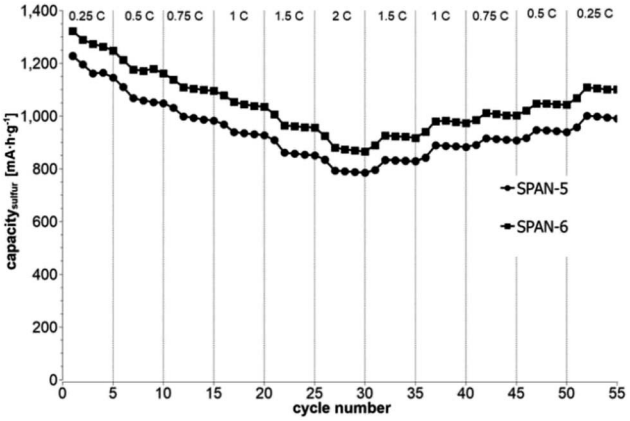

Fig. 6 Symmetrical stress test 0.25C–2C–0.25C of cells prepared from the TIPS-derived SPAN-based monoliths SPAN-5 and SPAN-6.

Table 3 Initial cycles of the different active materials at a discharge rate of 0.25C

	Initial discharge capacity [mA h g^{-1}]
SPAN-1	1416
SPAN-2	1478
SPAN-3	1560
SPAN-4	1601
SPAN-5	1671
SPAN-6	1721

(Fig. 8). These distinct differences in electrochemical performance deserve attention, the more since the materials are virtually chemically identical and the conductivity of all our (pressed) monolithic SPAN-materials is similar and $<10^{-8}$ S cm^{-1}. Conductivity of the parent material is thus somewhat lower than the one of particulate SPAN (10^{-6} S cm^{-1}),[42] which can be explained by the higher porosity of monolithic SPAN compared to particulate SPAN.

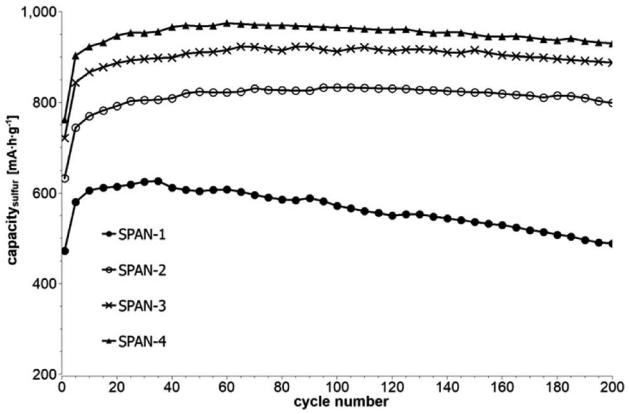

Fig. 7 Cycle test with 1C of cells prepared from the SIPS-derived SPAN-based monoliths SPAN-1 to SPAN-4.

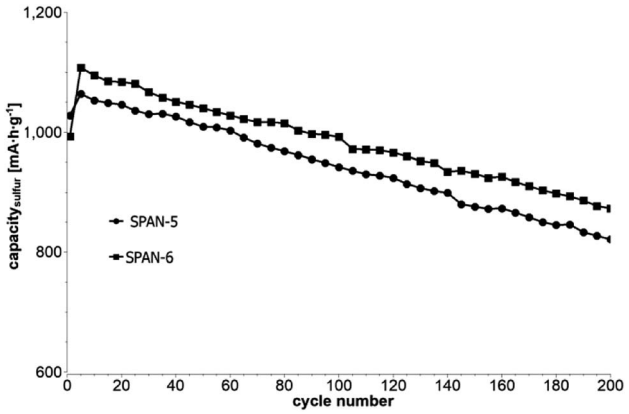

Fig. 8 Cycle test with 1C of cells based on the TIPS-derived SPAN-based monoliths SPAN-5 and SPAN-6.

Consequently, the differences in electrochemical performance must be a result of the materials' different microstructure. We attribute the high initial capacity of all SPAN monoliths is attributed to the small mesopores in the range of 3.5–4.2 nm that are present in SPAN as evidenced by N_2-sorption experiments (Fig. S7–S12, ESI†). These guarantee for a good wetting of the active material with the electrolyte. They also provide sufficient specific surface area ($14 < \sigma < 116$ m^2 g^{-1}) allowing substantial diffusion of lithium ions during reduction/oxidation to and from the SPAN-matrix. Such fast diffusion and mass transfer, respectively, is particularly important at higher C-rates. In addition to these small mesopores, there are also interparticle voids in the range of 100–1000 nm present, as confirmed by mercury porosimetry (Fig. S13–S18, Table S2†). These macropores guarantee for a sufficient amount of electrolyte. In addition, there is an irreversible reduction of the backbone of the SPAN-matrix in the first discharge cycle, which delivers higher discharge capacities. For SPAN-6 this results in a discharge capacity, which is even higher than the theoretical capacity of sulfur. This phenomenon is well-known for SPAN-based active materials.[17,38] The substantial differences in electrochemical performance between the individual active SPAN-

based materials SPAN-1 to SPAN-4 are attributed to the different monomer content in the monolithic PAN-precursor and, accordingly, in the corresponding monolithic SPAN. Obviously, percolation between the individual micrometer-sized structure-forming microglobules plays a major role, rendering SPAN-2 to SPAN-4, which have the highest monomer content, superior to all other materials, including the TIPS-derived ones, which are prepared from PAN/solvent mixtures with a comparably low polymer loading (PAN : solvent = 6 : 100 and 12 : 100, respectively, see Experimental section). In addition to the characterization of the monolithic SPAN-materials *via* mercury intrusion, nitrogen adsorption and SEM imaging, the tortuosity of the individual cathodes were measured *via* a Polarization-Interrupt-Experiment.[43,44] Tortuosity is not universally defined in literature, but a common definition is the ratio of the average pore length L_{eff} to the length of the porous medium L along the diffusion axis.[45] According to this the tortuosity τ is given by:

$$\tau = \frac{L_{\text{eff}}}{L} \quad (1)$$

During polarization of the cell, Li^+ ions are diffusing from the anode to the cathode. Once polarization is stopped, the cell relaxes and the Li^+-ions have to pass through the porous layer between the separators. The relaxation time t_r depends on the morphology and the average pore length L_{eff} of the active material. This way, tortuosity can be determined by measuring the relaxation time. Substitution of L_{eff} by t_r in eqn (1) gives the tortuosities listed in Table 4, which are calculated based on the relaxation time of the cells and the thickness of the coating.

The electrochemical behavior of the cells based on SIPS-derived SPAN-monoliths as active materials (SPAN-1 to SPAN-4) correlates with the determined tortuosities. The higher the tortuosity of the materials is, the lower the discharge capacities of the cells are (Fig. S22†). Furthermore, tortuosity of the active material correlates with the monomer content in the precursor PAN-monoliths. The less compact SPAN-monolith SPAN-1 shows the highest tortuosity (2.14) while the most compact monolith SPAN-4 possesses the lowest tortuosity (0.75). Compared to SIPS-derived SPAN-monoliths, TIPS-derived SPAN-monoliths generally showed high tortuosities, which is in view of the comparably low amounts of PAN used for their synthesis not surprising. Clearly, the low PAN : solvent ratios used TIPS-derived PAN-monoliths, lead to higher porosity and higher tortuosity. In addition, no crosslinking occurs in TIPS-derived SPAN-monoliths, which results in poor mechanical stability. Consequently, no clear correlation between electrochemistry and tortuosity can be achieved.

In view of its superior performance, the SPAN-4 monolith was additionally compared to a state-of-the-art fibrous SPAN cathode material reported earlier.[26,37] The comparison was done in form of a symmetrical stress test, starting at 0.5C with a maximum charge/discharge rate of 8C. It is remarkable that at a charge/discharge rate of 8C the SPAN-based monolith still outperformed the fibrous SPAN in terms of specific capacity (420 *vs.* 300 mA h g_{sulfur}^{-1},[26] Fig. S25, ESI†). Compared to fibrous SPAN, the monolithic SPAN showed a similar cycle behavior but reached higher discharge capacities at all C-rates (Table 5). Even at high C-rates up to 8C the coulombic efficiency of the cell was >99%.

Experimental section

Ethylene carbonate (EC, for electrochemistry, 99.9%, anhydrous), EC (for monolith synthesis, >98%), dimethyl carbonate (DMC, >99%, anhydrous), sulfur (99.5%, sublimed), cyano-2-propyl dodecyl trithiocarbonate (CPDT, >98%), 2,2′-azobis(2-methyl-propionitrile) (AIBN, >98%), poly(acrylonitrile) (PAN, M_n = 36 500 g mol^{-1}, PDI = 3.6), dimethyl sulfoxide (DMSO, 99%) and lithium bis(trifluoromethanesulfonyl)imide (LiTFSI, 99.95%) were purchased from Sigma-Aldrich (Munich, Germany). LiTFSI was dried *in vacuo* at 150 °C overnight prior to use. AIBN was recrystallized twice from methanol prior to use. Ethylene gycol dimethacrylate (EGDMA, >97%, TCI, Zwijndrecht, Belgium), acrylonitrile (AN, >99%, Merck, Darmstadt, Germany), Super C65 (Timcal, Bodio, Switzerland), poly(vinyl difluoride) (PVDF, Solvay, Brussels, Belgium), elemental lithium (>99.9%, Alfa Aesar, Karlsruhe, Germany) and *N*-methyl-2-pyrrolidone (NMP, >99.5%, TCI, Zwijndrecht, Belgium) were used as received.

The IR spectra were recorded on an IFS 128 ATR/FT-IR-spectrometer of Bruker in the range of 400 cm^{-1} to 4000 cm^{-1}. Scanning electron micrograph (SEM) images were recorded at the German Institutes of Textile and Fiber Research, DITF Denkendorf, using an Auriga type field emission scanning electron microscope from Zeiss. The samples were sputtered with Pt/Pd before measuring.

Table 4 Tortuosities of coatings based on SPAN1 to SPAN-6 as active materials

	Tortuosity τ
SPAN-1	2.14
SPAN-2	1.21
SPAN-3	0.98
SPAN-4	0.75
SPAN-5	1.34
SPAN-6	1.72

Table 5 Discharge capacities of cells based on fibrous SPAN (previous work[26]) and discharge capacities of a cell based on monolithic SPAN-4 at different C-rates (data from Fig. S25, ESI)

C-rate	$Capacity_{sulfur}$[22] (fibrous SPAN, mA h g^{-1})	$Capacity_{sulfur}$ (monolithic SPAN-4, mA h g^{-1})
0.5C	1040	1050
1C	950	990
2C	800	890
3C	650	790
4C	550	680
6C	350	500
8C	300	420

Synthesis of PAN-based monoliths *via* SIPS

Acrylonitrile (AN, 16 eq.), EGDMA (1 eq.), EC, ethanol (EtOH), CPDT, and AIBN were mixed in a vial and heated to 75 °C for 18 h. The concentration of the initiator and the RAFT-agent was the same in the synthesis of all monoliths (c(AIBN) = 0.78 mg mL^{-1} and c(CPDT) = 4 mg mL^{-1}). The solvent system and the ratio of solvents : monomers were varied in order to obtain four monoliths with different morphology. The composition of the solutions is shown in Table 1. After cooling to room temperature, all monoliths were washed with EtOH and dried *in vacuo*. Monoliths were characterized *via* nitrogen adsorption and desorption measurements and scanning electron microscopy (SEM).

Synthesis of PAN-based monoliths *via* TIPS

PAN (c(PAN) = 60 mg mL^{-1} for PAN-5 and 120 mg mL^{-1} for PAN-6) was dissolved within four hours in an DMSO/water mixture (vol/vol = 88 : 12) at 100 °C. After the solution was allowed to cool to room temperature, the obtained monoliths were washed several times with water and were freeze-dried. Monoliths were characterized *via* nitrogen adsorption and desorption measurements and SEM.

Synthesis of SPAN-monoliths

PAN-monoliths were converted into SPAN-monoliths *via* treatment with excess elemental sulfur at 550 °C for 5 h under a nitrogen atmosphere. Residual sulfur was removed after synthesis with toluene (Soxhlet extraction for 48 hours).[26] The resulting materials were characterized *via* elemental analysis and IR spectroscopy. The morphology of the SPAN-materials was characterized *via* SEM, nitrogen adsorption and desorption measurements and mercury porosimetry.

Electrochemistry

SPAN-monoliths were ground and sieved to achieve an average particle size < 63 μm. A dispersion of SPAN/Super C65/PVDF (70/15/15, wt%) in NMP was coated on a carbon-coated aluminum foil (200 μm_{wet}). The sulfur loading of the cathodes was 0.5 mg cm^{-2}. After drying at 60 °C, cathodes 12 mm in diameter were punched out of the sheet and transferred into an argon filled glovebox. Swagelok T-type cells were used for electrochemical characterization. Elemental lithium was used as anode, two Freudenberg FS 2190 membranes were used as separators and a freshly prepared 3 M solution of LiTFSI in EC/DMC (1 : 1) was used as electrolyte. All electrochemical measurements were performed on a BasyTec XCTS-LAB battery test station. The specific capacity and charge/discharge rates were calculated based on the mass of sulfur in the cathode (1C = 1672 mA h g^{-1}).

Tortuosity

Tortuosity was measured in a Polarization-Interrupt-Experiment.[43,44] For these purposes, the coating was removed from the current collector with an aqueous solution of sodium hydroxide and then washed several times with demineralized water. The coating was dried and sandwiched between two separators. For the measurements a symmetrical cell setup was used (Li *vs.* Li) with the separator-coating-separator sandwich in between. The electrolyte was 3 M LiTFSI in EC/DMC (1 : 1). The cells were polarized with 2 mA for two minutes, then the relaxation time was measured until the cell voltage reached 0 V (±0.0005 V).

Conclusions

We synthesized six different PAN-monoliths, both *via* solvent-induced and thermally-induced phase separation. All PAN-monoliths were characterized and converted into SPAN-monoliths through the reaction with elemental sulfur at 550 °C. In course of the conversion process the porous macroscopic, monolithic structure was preserved. A sulfur content around 40 wt% was reached throughout. Both the PAN- and SPAN-monoliths showed a defined structure in SEM and high specific surface areas up to 225 m^2 g^{-1}. The infrared spectra of the resulting SPAN monoliths as well as the atomic C : H and C : N ratios indicate the formation of the desired SPAN-structure. Conversion of monolithic PAN into monolithic SPAN proceeded under retention of the shape of the monolithic structure. Both the SIPS- and TIPS-derived SPAN monoliths allowed for the preparation SPAN-based Li–S cells. TIPS-derived SPAN monoliths performed poorly in terms of cycle stability. Our current explanation for this behavior relates to poor percolation and high tortuosities caused by a low monomer content. By contrast, SIPS-derived SPAN monoliths show high initial capacity and good cycle stability provided substantial percolation and lower tortuosities as is the case in SPAN-2 to SPAN-4. The electrochemical performance of monolithic SPAN materials correlates with tortuosity and even exceeds the one of fibrous SPAN reaching a specific capacity of up to 1330 mA h g_{sulfur}^{-1} @ 0.25C (sulfur utilization of 80%), 900 mA h g_{sulfur}^{-1} @ 2C (sulfur utilization of 54%) and 420 mA h g_{sulfur}^{-1} @ 8C (sulfur utilization of 25%).

Conflicts of interest

There are no conflicts to declare.

Acknowledgements

This work was financially supported by the German Federal Ministry for Economic Affairs and Energy (BMWi, project no. S50400). The authors wish to thank U. Hageroth and S. Henzler (DITF Denkendorf) for SEM measurements and M. Wieland (Institute of Polymer Chemistry, University of Stuttgart), J. Trueck (Daimler AG) and E. Hadjixenophontos (Institute of Materials Science, University of Stuttgart) for four-point-resistivity measurements.

References

1 A. Manthiram, Y. Fu, S. H. Chung, C. Zu and Y. S. Su, *Chem. Rev.*, 2014, **114**, 11751–11787.

2 X. Chen, T. Hou, K. Persson and A. Q. Zhang, *Mater. Today*, 2018, DOI: 10.1016/j.mattod.2018.04.007.
3 M. Wild, L. O'Neill, T. Zhang, R. Purkayastha, G. Minton, M. Marinescu and G. J. Offer, *Energy Environ. Sci.*, 2015, **8**, 3477–3494.
4 M. Arumugam, Y. Fu and A.-S. Su, *Acc. Chem. Res.*, 2013, **46**, 1125–1134.
5 M. R. Busche, P. Adelhelm, H. Sommer, H. Schneider, K. Leitner and J. Janek, *J. Power Sources*, 2014, **259**, 289–299.
6 B. Zhang, X. Qin, G. R. Li and X. P. Gao, *Energy Environ. Sci.*, 2010, **3**, 1531.
7 X. Li, Y. Cao, W. Qi, L. V. Saraf, J. Xiao, Z. Nie, J. Mietek, J.-G. Zhang, B. Schwenzer and J. Liu, *J. Mater. Chem.*, 2011, **21**, 16603.
8 J. S. Lee, W. Kim, J. Jang and A. Manthiram, *Adv. Energy Mater.*, 2017, **7**, 1601943.
9 Y. S. Su, Y. Fu and A. Manthiram, *Phys. Chem. Chem. Phys.*, 2012, **14**, 14495–14499.
10 J. Wang, J. Yang, J. Xie and N. Xu, *Adv. Mater.*, 2002, **14**, 963–965.
11 W. Wang, Z. Cao, G. A. Elia, Y. Wu, W. Wahyudi, E. Abou-Hamad, A.-H. Emwas, L. Cavallo, L.-J. Li and J. Ming, *ACS Energy Lett.*, 2018, **3**, 2899–2907.
12 J. Wang, J. Yang, C. Wan, K. Du, J. Xie and N. Xu, *Adv. Funct. Mater.*, 2003, **13**, 487–492.
13 X. Yu, J. Xie, J. Yang, H. Huang, K. Wang and Z. Wen, *J. Electroanal. Chem.*, 2004, **573**, 121–128.
14 J. Fanous, M. Wegner, J. Grimminger, Ä. Andresen and M. R. Buchmeiser, *Chem. Mater.*, 2011, **23**, 5024–5028.
15 J. Fanous, M. Wegner, M. B. M. Spera and M. R. Buchmeiser, *J. Electrochem. Soc.*, 2013, **160**, A1169–A1170.
16 J. Fanous, M. Wegner, J. Grimminger, M. Rolff, M. B. M. Spera, M. Tenzer and M. R. Buchmeiser, *J. Mater. Chem.*, 2012, **22**, 23240–23245.
17 S. Zhang, *Energies*, 2014, **7**, 4588–4600.
18 S. Wei, L. Ma, K. E. Hendrickson, Z. Tu and L. A. Archer, *J. Am. Chem. Soc.*, 2015, **137**, 12143–12152.
19 S. Warneke, A. Hintennach and M. R. Buchmeiser, *J. Electrochem. Soc.*, 2018, **165**, A2093–A2095.
20 Z. Chen, J. Zhou, Y. Guo, C. Liang, J. Yang, J. Wang and Y. Nuli, *Electrochim. Acta*, 2018, **282**, 555–562.
21 L. Wang, X. He, J. Li, J. Gao, J. Guo, C. Jiang and C. Wan, *J. Mater. Chem.*, 2012, **22**, 22077.
22 C.-F. J. Kuo, M. A. Weret, H.-Y. Hung, M.-C. Tsai, C.-J. Huang, W.-N. Su and B.-J. Hwang, *J. Power Sources*, 2019, **412**, 670–676.
23 Y. X. Yin, S. Xin, Y. G. Guo and L. J. Wan, *Angew. Chem., Int. Ed.*, 2013, **125**, 13426–13441.
24 S. Warneke, R. K. Zenn, T. Lebherz, K. Müller, A. Hintennach, U. Starke, R. E. Dinnebier and M. R. Buchmeiser, *Adv. Sustainable Syst.*, 2018, **2**, 1700144.
25 W. Pu, X. He, L. Wang, Z. Tian, C. Jiang and C. Wan, *Ionics*, 2007, **13**, 273–276.
26 M. Frey, R. K. Zenn, S. Warneke, K. Müller, A. Hintennach, R. E. Dinnebier and M. R. Buchmeiser, *ACS Energy Lett.*, 2017, **2**, 595–604.
27 M. R. Buchmeiser, *Angew. Chem., Int. Ed.*, 2001, **113**, 3911–3913.
28 M. R. Buchmeiser, *Polymer*, 2007, **48**, 2187–2198.
29 J. M. J. Frechet and F. Svec, *Anal. Chem.*, 1992, **64**, 820–822.
30 F. Svec and J. M. J. Frechet, *Macromolecules*, 1995, **28**, 7580–7582.
31 K. Okada, M. Nandi, J. Maruyama, T. Oka, T. Tsujimoto, K. Kondoh and H. Uyama, *Chem. Commun.*, 2011, **47**, 7422–7424.
32 W. Gang, J. Wang, H. Zhang, Z. Fei, T. Wu, Q. Ren and J. Qiu, *Chem. Eng. J.*, 2016, **313**, 1607–1614.
33 J. M. Spörl, A. Ota, R. Beyer, T. Lehr, A. Müller, F. Hermanutz and M. R. Buchmeiser, *J. Polym. Sci., Part A: Polym. Chem.*, 2014, **52**, 1322–1333.
34 H. O. Desseyn, B. J. Van Der Veken and M. A. Herman, *Appl. Spectrosc.*, 1978, **32**, 101–105.
35 M. Antonietti, N. Fechler and T.-P. Fellinger, *Chem. Mater.*, 2013, **26**, 196–210.
36 Y. S. Hu, P. Adelhelm, B. M. Smarsly, S. Hore, M. Antonietti and J. Maier, *Adv. Funct. Mater.*, 2007, **17**, 1873–1878.
37 S. Warneke, M. Eusterholz, R. K. Zenn, A. Hintennach, R. E. Dinnebier and M. R. Buchmeiser, *J. Electrochem. Soc.*, 2017, **165**, A6017–A6020.
38 S. Warneke, M. Eusterholz, R. K. Zenn, A. Hintennach, R. E. Dinnebier and M. R. Buchmeiser, *J. Electrochem. Soc.*, 2017, **165**, A6017–A6020.
39 D. Zheng, D. Liu, J. B. Harris, T. Ding, J. Si, S. Andrew, D. Qu, X.-Q. Yang and D. Qu, *ACS Appl. Mater. Interfaces*, 2017, **9**, 4326–4332.
40 R. Xu, J. Lu and K. Amine, *Adv. Energy Mater.*, 2015, **5**, 1500408.
41 M. Safari, C. Y. Kwok and L. F. Nazar, *ACS Cent. Sci.*, 2016, **2**, 560–568.
42 L. Yin, J. Wang, F. Lin, J. Yang and Y. Nuli, *Energy Environ. Sci.*, 2012, **5**, 6966–6972.
43 D. Kehrwald, P. R. Shearing, N. P. Brandon, P. K. Sinha and S. J. Harris, *J. Electrochem. Soc.*, 2011, **158**, A1393–A1399.
44 N. A. Zacharias, D. R. Nevers, C. Skelton, K. Knackstedt, D. E. Stephenson and D. R. Wheeler, *J. Electrochem. Soc.*, 2013, **160**, A306–A311.
45 N. Epstein, *Chem. Eng. Sci.*, 1989, **44**, 777–779.